Online treatment of eruption dynamics improves the volcanic ash and SO_2 dispersion forecast: case of the Raikoke 2019 eruption

Julia Bruckert[1], Gholam Ali Hoshyaripour[1], Ákos Horváth[2], Lukas O. Muser[1], Fred J. Prata[3], Corinna Hoose[1], and Bernhard Vogel[1]

[1]Institute of Meteorology and Climate Research, Karlsruhe Institute of Technology (KIT), Karlsruhe, Germany
[2]Meteorological Institute, University of Hamburg, Germany
[3]AIRES Pty. Ltd., Mt Eliza, Victoria, Australia

Correspondence: Julia Bruckert (julia.bruckert@kit.edu)

Abstract. In June 2019, the Raikoke volcano, Kuril Islands, emitted 0.4-1.8 x 10^9 kg of very fine ash and 1-2 x 10^9 kg of SO_2 up to 14 km into the atmosphere. The eruption was characterized by several eruption phases of different duration and height summing up to a total eruption length of about 5.5 h. Resolving such complex eruption dynamics is required for precise volcanic plume dispersion forecasts. To address this issue, we coupled the atmospheric model system ICON-ART (ICOsahedral Nonhydrostatic – Aerosols and Reactive Trace gases) with the 1-D plume model FPlume to calculate the eruption source parameters (ESPs) online. The main inputs are the plume heights for the different eruption phases that are geometrically derived from satellite data. An empirical relationship is used to derive the amount of very fine ash (particles <32μm), which is relevant for long range transport in the atmosphere. On the first day after the onset of the eruption, the modeled ash loading agrees very well with the ash loading estimated from AHI (Advanced Himawari Imager) observations due to the resolution of the eruption phases and the online treatment of the ESPs. In later hours, aerosol dynamical processes (nucleation, condensation, coagulation) explain the loss of ash in the atmosphere in agreement with the observations. However, a direct comparison is partly hampered by water and ice clouds overlapping the ash cloud in the observations. We compared 6-hourly means of model and AHI data with respect to the structure, amplitude, and location (SAL-method) to further validate the simulated dispersion of SO_2 and ash. In the beginning, the structure and amplitude values for SO_2 differed largely because the dense ash cloud leads to an underestimation of the SO_2 amount in the satellite data. On the second and third day, the SAL values are close to zero for all parameters (except for the structure value of ash) indicating a very good agreement of model and observations. Furthermore, we found a separation of the ash and SO_2 plume after one day due to particle sedimentation, chemistry, and aerosol-radiation interaction.

The results confirm that coupling the atmospheric model system and plume model enables detailed treatment of the plume dynamics (phases and ESPs) and leads to significant improvement of the ash and SO_2 dispersion forecast. This approach can benefit the operational forecast of ash and SO_2 especially in case of complex and non-continuous volcanic eruptions like the Raikoke 2019.

1 Introduction

Explosive volcanic eruptions inject particulate matter and gases into the atmosphere, which are then dispersed by atmospheric transport processes. Volcanic ash can remain airborne for up to a few months (e.g., Robock, 2000; Niemeier et al., 2009; Jensen et al., 2018) and drift away several thousand kilometers from the eruption point when emitted into the lower stratosphere or higher. Moreover, oxidation of volcanogenic SO_2 leads to formation of sulfate particles as secondary volcanic aerosols. These aerosols enhance the scattering of sunlight in the atmosphere and, thus, reduce the incoming shortwave radiation reaching the ground (e.g., Robock, 2000). Therefore, while the dispersion of ash particles mainly matters for aviation safety (Casadevall, 1994), regional public health (Horwell and Baxter, 2006), and local environment and infrastructure (e.g., Spence et al., 2005; Stewart et al., 2006; Wardman et al., 2012), the fate of SO_2 is crucial for predicting the impacts of volcanism on weather and climate (Robock, 2000; Mather, 2008; Timmreck, 2012; von Savigny et al., 2020).

Forecasting the dispersion of volcanic aerosols in the atmosphere relies on the representation of both the source and sink parameters and processes. It has been shown that eruption source parameters (ESP) such as mass eruption rate (MER), plume height, emission profile, and the duration of the eruption can strongly influence the quality of the forecast of the spatial distribution of the volcanogenic gases and particles (e.g., Scollo et al., 2008; Harvey et al., 2018). The plume height can be estimated instantaneously by visual, radar, and lidar based or satellite observations. Until a few hours after the onset of a volcanic eruption when such plume height observations become available, MER usually remains uncertain. Estimates of the MER include empirical parametrizations based on plume height (e.g., Mastin et al., 2009) partially corrected by wind effects (e.g., Degruyter and Bonadonna, 2012; Woodhouse et al., 2013) or are derived with 1D plume models (e.g., Folch et al., 2016). Further uncertainties arise from the choice of the eruption profile (e.g., De Leeuw et al., 2020), i.e., the vertical distribution of mass. Different approaches exist to parameterize the emission profile, e.g., idealized profiles (Stuefer et al., 2012), plume-theory-based profiles (Marti et al., 2017), Gaussian-shaped profiles derived from backward trajectory modeling (Rieger et al., 2015), constant profiles (e.g., Beckett et al., 2020; Muser et al., 2020, hereafter M20), or more complex ones derived from the observations (e.g., De Leeuw et al., 2020). However, in all parametrizations of the ESPs the volcanic plume dispersion remains decoupled from unresolved volcanic eruption dynamics including also the influence of the atmosphere on the emission height. This accounts for large uncertainties in modeling studies at regional to global scales (Textor et al., 2005; Timmreck, 2012; von Savigny et al., 2020). Marti et al. (2017) overcame this issue by coupling the NMMB-MONARCH-ASH transport model (Nonhydrostatic Multiscale Model on the B-grid – Multiscale Online Nonhydrostatic AtmospheRe CHemistry model – ASH) with the 1D plume model FPlume, which calculates the MER and the mass distribution in the column online. Another example is the study by Collini et al. (2013), who combined the WRF/ARW forecast system with FALL-3D and highlighted a good agreement in ash transport simulations with satellite observations for the Cordon Caulle eruption 2011. Plu et al. (2021) simulated the 2010 Eyjafjallajökull eruption with MOCAGE model (Modèle de Chimie Atmosphérique de Grande Echelle) and hourly changing MER from FPlume. They highlighted more concentrated ash concentrations in the horizontal and vertical scale, which more realistically represents the horizontal dispersion compared to parameterized MERs.

Only ash particles smaller than 32 μm (hereafter referred to as very fine ash) are relevant for long range transport in the atmosphere (Rose and Durant, 2009). However, the amount of very fine ash emitted by a volcanic eruption is uncertain and depends on different parameters such as the strength and height of an eruption (Gouhier et al., 2019), the composition of magma (Rose and Durant, 2009), and the availability of water (e.g., van Eaton et al., 2012; Prata et al., 2017). Gouhier et al. (2019) analyzed data of past volcanic eruptions with respect to the fraction of very fine ash in the whole mass erupted. They found that strong volcanic eruptions are less efficient in emitting very fine ash into the atmosphere possibly due to higher sedimentation within the plume. Most forecast models assume a fixed value for the fraction of very fine ash between 1% (e.g., M20) and 5% (e.g., Webster et al., 2012; Beckett et al., 2020) regardless of the strength of the eruption and lava composition.

Once emitted into the atmosphere, aerosol dynamics (including aggregation) lead to a faster growth of particles and, thus, a quicker removal from the atmosphere (e.g., Brown et al., 2012, and references therein). M20 investigated the impacts of aerosol dynamics and radiation interactions on the ash dispersion after the Raikoke eruption in June 2019. They showed that aerosol dynamical processes such as nucleation, condensation, and coagulation enhance the removal of the ash particles from the atmosphere. On the other hand, the absorption of incoming shortwave radiation by internally mixed aerosols leads to the lofting of the aerosol plume. The simulated lofting effect for the Raikoke eruption resulted in a 6 km rise of the plume top after the first 4 days (M20). Zhu et al. (2020) confirmed that coagulation of mixed particles with ash and sulfate is required to produce the evolution of the size distribution of mixed particles following the Kelud eruption 2014. However, they further found that the initial SO_2 lifetime is determined by direct SO_2 uptake on ash, rather than its oxidation by OH.

Here, we aim to link complex ESPs during the first hours of volcanic eruptions to the fate of volcanogenic gases and aerosols. As a case study, we investigate the ash and SO_2 dispersion of the Raikoke eruption (48.29°N, 153.24°E) on 21 and 22 June, 2019 during the first three days after the eruption onset. The eruption was characterized by ten eruption phases of 5 to 14 km height lasting between 5 min and 3 h (Horváth et al., 2021b). Such complexity leads to further difficulties in deriving reasonable ESPs for plume dispersion forecasts. Throughout the paper, we define 'eruption phase' as one distinct time period in which the volcano was erupting. The constant emission rate and profile used by M20 caused an approximately 6 h time lag between the time series of modeled and observed ash mass loading. This gap might be filled by improving the representation of the ESPs and a varying very fine ash fraction according the relationship by Gouhier et al. (2019). Moreover, the impacts of source and sink processes on the fate of SO_2 erupted from Raikoke remain unexplored in the study by M20. Kloss et al. (2021) investigate SO_2 transport following the Raikoke 2019 eruption with observations and models. They found enhanced stratospheric aerosol optical depths in the whole northern hemisphere for more than one year following the Raikoke eruption when using an SO_2 setup which realistically represents the transport of volcanic compounds during the first hours after the Raikoke eruption. De Leeuw et al. (2020) found that simulating the correct burden of SO_2 is sensitive to the fraction emitted into the lower stratosphere and therefore depends strongly on the emission profile chosen. In this work, we want to answer the following research questions: How large is the influence of resolving the eruption phases on the predicted ash mass loading after the Raikoke eruption? Can an online treatment of volcanic ESPs improve the predicted mass loading and dispersion of ash and SO_2 plumes? And what is the impact of aerosol–radiation interaction on the dispersion of the SO_2 plume? The paper is structured as follows: in Sect. 2, the methodology including the model setup, the inputs, observations, and the validation

method used are described. In Sect. 3, we evaluate our experiments with respect to mass loading and structure, amplitude, and location of the plume. In addition, we discuss the separation of the ash and SO_2 plumes due to aerosol-radiation interaction. Finally, Sect. 4 concludes the paper.

2 Methods

2.1 ICON-ART modeling system

In this study, we performed simulations with the global weather and climate model ICON (ICOsahedral Nonhydrostatic model) together with the module for Aerosol and Reactive Trace gases (ART). ICON solves the full three-dimensional non-hydrostatic and compressible Navier-Stokes equations on an icosahedral grid and allows seamless predictions from local to global scales (Zängl et al., 2015; Heinze et al., 2017; Giorgetta et al., 2018).

ART, being part of ICON, supplements the model by including emissions, transport, gas phase chemistry, and aerosol dynamics in the troposphere and stratosphere (Rieger et al., 2015; Weimer et al., 2017; Schröter et al., 2018). M20 reported and demonstrated latest improvements in ICON-ART with respect to the AEROsol DYNamics module (AERODYN), which is also used in the present paper. In AERODYN, aerosols are organized in seven log normal distributions considering Aitken (as soluble), accumulation (as soluble, insoluble and mixed), coarse (as insoluble and mixed) and a giant mode (as insoluble). For each mode, the prognostic equations for number density and mass concentration are solved keeping the standard deviations of the modes constant. For the Aitken mode, nucleation, condensation, and coagulation are considered, while accumulation mode and coarse mode are affected by condensation and coagulation only. Shifting of particles into another mode occurs either when a threshold diameter is exceeded (shift into larger mode) or when a mass threshold of soluble coating on insoluble particles is exceeded (shift from insoluble to mixed mode) (M20). In AERODYN, water and sulfate (also ammonium and nitrate) can condense on ash particles and therefore change the physical properties of ash, e.g., size, density, optical properties. Changes of particle optical properties can further feedback on the radiation and atmospheric state. However, effects of aerosol dynamics on atmospheric humidity and clouds is not considered yet.

For detailed descriptions of ICON, ART, and AERODYN, we here refer to the works by Zängl et al. (2015), Rieger et al. (2015) and Schröter et al. (2018), and M20, respectively.

2.2 Coupling ICON-ART with FPlume

For a better estimation of the ESPs, we coupled ICON-ART online with the one-dimensional volcanic plume rise model FPlume (Folch et al., 2016; Macedonio et al., 2016). FPlume solves the equations of the buoyant plume theory (Morton et al., 1956) along the vertical plume axis. It includes processes like ambient air entrainment, plume bending due to wind, particle wet aggregation, energy supply due to water phase changes, particle fallout, and re-entrainment of particles (Folch et al., 2016).

Figure 1 summarizes the procedures performed at every time step in which FPlume is active: First, vertical profiles for wind, temperature, pressure, and humidity simulated with ICON serve as meteorological inputs for FPlume. In the second step,

FPlume calculates the plume properties, i.e, total MER in case of a given plume height (as here) or plume height in case of a given MER. Thirdly, the fraction of very fine ash is determined based on plume height and total MER by using the relationship of Gouhier et al. (2019).

In the last step, ash is emitted into ICON-ART by multiplying the MER of very fine ash with the vertical profile derived from the normalized Suzuki distribution, which is the same as the one used by Marti et al. (2017):

$$S^*(z) = \frac{\mathrm{E}\left(\left(1-\frac{z}{H_p}\right)\exp\left(4.0\left(\frac{z}{H_p}-1\right)\right)\right)^{5.0}}{MAX(S(z))} \quad (1)$$

Here, $S(z)$ is the numerator of the equation and describes the vertical emission profile, E is the emission rate of very fine ash, H_p is the plume top height, and z refers to the height in the plume. Eq. 1 explains the shape of the emission profile used here, which is also plotted in Fig. A1 in comparison with other profiles. To ensure the correct total ash mass emission and units when the particles are released into ICON-ART at discrete point sources in each model layer between the bottom and top height of the plume, we further normalized Eq. 1 by the vertical integral of $S^*(z)$ (Rieger et al., 2015). We completely disregarded the mass of particles larger than 32 μm as this fraction has been shown to be irrelevant for long-range transport (Rose and Durant, 2009).

More details on the initialization of the ash particles is given in the next section. Besides ash, we also emitted SO_2. Different from the ash emission, we prescribed the MER of SO_2 based on satellite estimates, but we released it into ICON-ART with the same profile and phases as the ash. This simplification was necessary as no further information on temporally SO_2 emission is available. Yet, during volcanic eruptions in general it is possible that the ash and SO_2 are emitted at different phases of the eruption (e.g., Thomas and Prata, 2011).

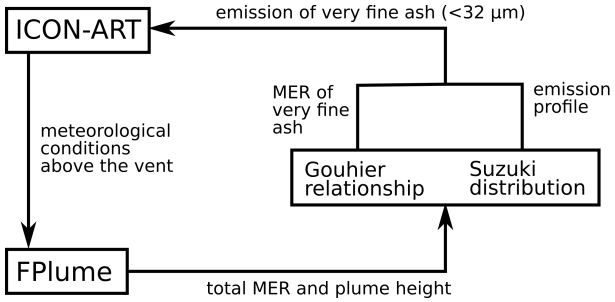

Figure 1. Schematic of the setup with the coupling between the global ICON-ART model and the 1D-plume rise model FPlume.

Besides meteorological data, FPlume needs estimates of the exit temperature, exit velocity, exit volatile fraction, and plume height to solve for the total MER. Our setup enables to define these parameters for multiple eruption phases meaning that the MER used for ICON-ART depends on the exit conditions for each plume phase and the meteorological conditions. When solving the plume dynamics for the MER knowing the plume height, FPlume performs the calculations iteratively for a range of possible MERs to reach the plume height wanted (Folch et al., 2016).

2.2.1 Separation of the volcanic plume from the background

To study the evolution of the ash and SO_2 plume in the atmosphere following the Raikoke eruption, we had to separate the ash and SO_2 volcanic plume from the background mixing ratios due to technical reasons. In ICON-ART, we initialized the ash modes with 100 particles per kg air to avoid a division by zero in the diameter calculation routines. Thus, to study especially the behavior of the plume top, we used the following mixing ratio thresholds above which a grid cell is considered as inside the plume, and which are based on M20: 0.01 $\mu\mathrm{gkg}^{-1}$, 1 $\mu\mathrm{gkg}^{-1}$, and 100 $\mu\mathrm{gkg}^{-1}$ for the accumulation, coarse, and giant mode, respectively. The corresponding threshold of SO_2 is 10 ppm.

2.3 Eruption source parameters

2.3.1 Vent conditions

Raikoke emits primary basaltic lava, and, therefore, we assumed the following exit conditions for FPlume: The exit temperature of 1273 K and exit water mass fraction of 3% were the same for all eruption phases (Mastin, 2007); the exit velocity of the individual phase ve_{ph} was a linear function of the plume height above the vent H_{ph} between 14000 m and 4000 m, where the exit velocity was set to 150 ms^{-1} and 90 ms^{-1}, respectively. Thus, the following equation calculates ve_{ph} based on H_{ph} in m:

$$ve_{ph} = 6\mathrm{s}^{-1}\frac{H_{ph}}{1000} + 66\mathrm{ms}^{-1} \quad (2)$$

The resulting MERs are insensitive to the input vent conditions (temperature, velocity, volatile fraction) in the range of 10%.

The equation for the very fine ash fraction by Gouhier et al. (2019) depends on whether the SiO_2 content is high or low and whether the conduit was opened or closed. As no information on the conduit has been available so far, we averaged the very fine ash fraction for low SiO_2 – closed conduit and low SiO_2 – opened conduit.

2.3.2 Geometric plume heights

In addition to temperature and exit velocity, FPlume requires the plume height as input to calculate the MER. The height above the Earth ellipsoid of the individual eruption phases was estimated by a recently developed geometric technique (Horváth et al., 2021a), which exploits the near-limb views provided by Geostationary Operational Environmental Satellite-17 (GOES-17). Such oblique observations offer close to orthogonal side views of vertical columns protruding from the Earth ellipsoid and thereby facilitate a simple height-by-angle method to derive point estimates of eruption column height in the vicinity of the vent. The GOES-17 side view heights were in good agreement with independent geometric estimates derived from plume shadows and GOES-17–Himawari-8 stereo observations (Horváth et al., 2021b).

The Raikoke plume heights cannot be unambiguously determined by the traditional infrared brightness temperature method. For most eruption phases, the minimum 11 μm brightness temperature (BT_{11}) falls within the narrow temperature range of the quasi-isothermal layer above the tropopause and leads to multiple height solutions within a wide altitude range of 10-24 km. At certain times (e.g., 23:50 UTC on 21 June or 01:20 UTC on 22 June), the massive eruption plume is undercooled, even

precluding the application of the temperature method. For the smaller plumes produced by less energetic eruption phases, on the other hand, the BT_{11} has a warm bias due to contributions from the warmer lower-level marine stratocumulus cloud layer around the volcano, resulting in underestimated heights. A detailed analysis of the Raikoke plumes, including a comparison of the various height estimates, is given in Horváth et al. (2021b). The uncertainty of the plume heights lays within a range of ± 500 m. As FPlume requires the plume height above the vent, we converted the GOES-17 above-ellipsoid heights by subtracting a vent height of 550 m.

2.4 Model configuration

We performed global simulations with ICON-ART using a horizontal grid size of roughly 13.2 km (R3B07 grid) and 90 vertical levels up to 75 km. The global icosahedral grid of ICON ensures a uniform resolution across the globe. For each experiment, we simulated 72 h starting from June 21, 12.00 UTC with initialized analysis data provided by the German Meteorological Service (DWD). During active eruption periods, the ESPs of Raikoke are calculated online with FPlume.

The 2019 Raikoke eruption was characterized by 9 shorter eruption phases between 18 UTC on June 21 and 7 UTC on June 22 and one more or less continuous eruption phase between 22.40 UTC and 01.55 UTC. We performed three experiments: 1) a reference experiment in which FPlume calculates ESPs with a varying very fine ash fraction and aerosol-radiation interaction activated in ICON-ART (FPlume-rad, Table 1); 2) the second experiment calculates the ESPs same as above, but neglects the interaction of aerosols and radiation (FPlume-norad). The comparison of FPlume-rad and FPlume-norad allows to quantify the lifting of the volcanic plume due to radiation; 3) the third experiment derives ESPs with the empirical relationship by Mastin et al. (2009), and it emits volcanic compounds with a prescribed very fine ash fraction from the reference case (mean value for each phase) along a Suzuki profile (i.e., Eq. 1). It further assumes aerosol-radiation interaction (Mastin-rad). The experiments FPlume-rad and FPlume-norad calculate the ESPs online within the simulation, whereas in Mastin-rad the ESPs are derived offline independent of the atmosphere and vent conditions. Table 1 summarizes the prescribed input parameters for the FPlume-rad experiment associated with the different eruption phases, which are fixed for the individual phases. The time limits for the phases and plume heights above the vent are based on satellite images from GOES-17, which are described in Sect. 2.3.2. Due to the 10-minute temporal resolution of the GOES-17 data, the uncertainty in the start and end time of each individual eruption phase is smaller than ± 5 min.

Figure 2 shows the MER of very fine ash that is released into ICON-ART by FPlume (red dots) and the Mastin relationship (blue dots). The fraction of very fine ash relative to the total MER predicted by FPlume is in the order of 1.5 - 3 % (not shown). In most phases, the MER calculated with FPlume is lower than the MER calculated with the Mastin equation, and the difference tends to be higher for larger plume heights. Since the exit parameters are fixed during each phase in the reference case, variation of the MER derived by FPlume must be due to changes in the atmospheric conditions. As the relationship by Mastin et al. (2009) neglects atmospheric conditions and the very fine ash fraction is fixed within one phase, the MERs of the very fine ash are constant within each phase. The vertical profiles of the meteorological variables in Fig. A2a indicate increasing temperatures in most levels below 10 km during the long eruption phase between 9 and 14 h after simulation start. Additionally, the specific humidity increases by up to 1 g kg^{-1} in the lower 2 km (Fig. A2c). When warmer and moist air is

Table 1. Model setup and input parameters for the individual eruption phases (FPlume-rad). The definition of the phases and plume heights above sea level (a.s.l.) are based on GOES-17 satellite observation as described in sect. 2.3.2. The exit conditions are based on typical values of basaltic eruptions as described in Sect. 2.3.1. The SO_2 mass emission rate is based on an observational estimate of the total SO_2 mass following the 2019 Raikoke eruption from M20, which was distributed over the individual phases with Eq. 3 . This table only shows the values that are predefined and fixed for the individual phases. The temporally varying MER of the very fine ash, which is derived with FPlume and the relationship by (Gouhier et al., 2019), and which is released into ICON-ART, is shown in Fig. 2.

Phase number	Date	Time in UTC	Plume height in m (a.s.l.)	Exit temperature in K	Exit velocity in m s^{-1}	Exit volatile fraction in %	SO_2 mass emission rate in kg s^{-1}
01	June 21	17.55-18.20	7250	1273	106	3	43865
02	June 21	18.50-19.05	9250	1273	118	3	56960
03	June 21	19.40-20.05	10250	1273	124	3	63507
04	June 21	20.40-20.50	9250	1273	118	3	56960
05	June 21	21.20-21.25	10250	1273	124	3	63507
06	June 21/22	22.00-22.05	11750	1273	133	3	73327
07	June 22	22.40-01.55	13750	1273	145	3	86421
08	June 22	03.40-04.05	11750	1273	133	3	73327
09	June 22	05.40-05.55	13250	1273	142	3	83148
10	June 22	07.00-07.10	4750	1273	91	3	27498

entrained into the plume, the plume density reduces faster due to the lower ambient air density and the release of latent heat. This effect results in a higher positive buoyancy and a lower MER to reach a fixed height. In addition, the wind speed decreases in the lower 4 km between 9 and 14 h after simulation start, which reduces the plume bending and subsequently the MER needed to reach a fixed height.

According to the MER values in Fig. 2, the total mass of very fine ash emitted in the model for all eruption phases together is about $1.21 \cdot 10^9$ kg using FPlume and $1.48 \cdot 10^9$ kg using Mastin-derived MERs.

The total mass of very fine ash is evenly distributed as insoluble tracer over the accumulation, coarse, and giant modes. The three insoluble modes are emitted as lognormal distributions with median diameters of 0.8, 2.98, and 11.35 μm, respectively. The standard deviation is 1.4 for each mode.

Following previous studies, we emitted a total of $1.5 \cdot 10^9$ kg SO_2 (M20; Kloss et al., 2020; De Leeuw et al., 2021). However, the SO_2 release is linearly adjusted to the eruption heights and length of each phase (Table 1) as follows:

$$E_{ph} = \overline{E}_{SO2} \cdot \frac{H_{ph}}{H_T} \tag{3}$$

E_{ph} is the phase-dependent MER of SO_2, $\overline{E}_{SO2}$ is the mean MER based on the observed amount of SO_2 and the sum of the duration of all phases, H_{ph} is the phase plume height (above the vent), and $H_T = 11571.2$ m is the phase duration-weighted

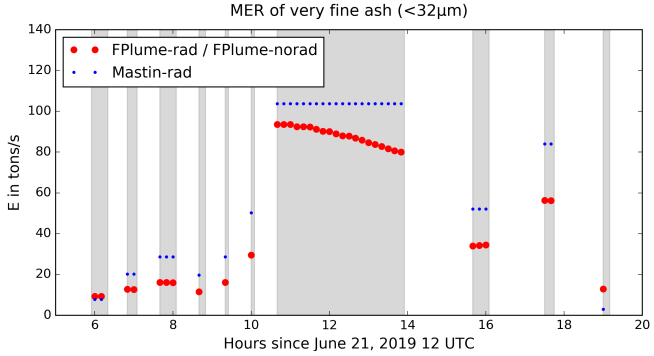

Figure 2. Mass eruption rate E for very fine ash in tons/s calculated with FPlume MER times the very ash fraction from Gouhier et al. (2019) (red) and calculated with Mastin MER times the very fine ash fraction derived in the FPlume experiment (blue). The very fine ash fraction is the same in both experiments to allow a direct comparison of the FPlume and Mastin derived MER on the dispersion in the atmosphere. Active eruption phases are indicated by the gray shading.

(t) mean plume height derived as:

$$H_T = \frac{\sum_{i=1}^{10} H_{ph,i} \cdot t_i}{\sum_{i=1}^{10} t_i} \tag{4}$$

Finally, SO_2 release is vertically distributed according to the Suzuki profiles (comparison to previously used profiles in Fig. A1). Here, ICON-ART treats SO_2 as a chemical tracer that can be oxidized by a simplified OH-chemistry scheme as presented in Weimer et al. (2017).

2.5 Himawari-8 Ash and SO_2 retrievals

To validate the model results, we used column SO_2 and ash mass loadings estimated from the 16-band visible and infrared Advanced Himawari Imager (AHI) onboard the Himawari-8 geostationary satellite at every full hour. Himawari-8 is operated by the Japanese Space Agency (JAXA) and the Japanese Meteorological Agency (JMA). A detailed description of the data product and methods used here is already given in M20 and references therein. In short, SO_2 is retrieved by the AHI band centered near 7.3 μm, where the absorption of SO_2 is high. A further retrieval scheme, as described in Prata et al. (2004), was applied to minimize the interference with vapor and clouds. For volcanic ash retrievals, the AHI bands near 11.2 μm and 12.4 μm are considered. The lower detection threshold is <0.2 g m^{-2} for volcanic ash. The ash retrievals were corrected by a mask that accounts for pixels that contain meteorological clouds but which were classified as completely cloud covered. Hereby, only pixels inside a 0.1 g m^{-2} contour line are considered and a 9x9 median filter smooths out 'spikes'.

2.6 SAL Method

The SAL method is an object-based quality measure originally developed to verify precipitation forecasts (Wernli et al., 2008, 2009). However, it has also been successfully applied for transport forecasts of volcanic compounds (e.g., M20; De Leeuw et al., 2021) and was used in this study for volcanic ash and SO_2 as well. The SAL method evaluates modeled and observed data according to their structure (S), amplitude (A), and location (L). While it assesses predefined objects based on a threshold value for the S and L component, the A component is a normalized domain-averaged quantity. The structure component S compares model and observations with respect to the volume of the defined objects. The value ranges between -2 and 2. Positive values indicate too large and/or too flat objects, whereas negative values indicate too small and/or too peaked objects. A value of 0 refers to a perfect forecast with respect to the structure. The amplitude component A evaluates the domain-averaged relative deviation of the forecasts from observations, and it is positive when the model overestimates the predicted quantity and vice versa (it also ranges between -2 and 2). For a perfect forecast of the amplitude, A is zero. The location component L consists of two parts: L1 describes the agreement between forecast and observation in terms of the normalized difference between the centers of mass, whereas L2 refers to the average distance between the center of mass of all objects and the individual objects. Each of L1 and L2 can reach values between 0 and 1 so that L in total can have values between 0 and 2 with a perfect forecast with respect to the location at L=0 (Wernli et al., 2008, 2009).

For SAL comparison of Himawari-8 and ICON-ART data, we derived 6-hour averages from both data sets at every full hour. Furthermore, we interpolated ash and SO_2 values onto a regular grid between 120° W and 80° E and 20° N and 85° N with a resolution of 0.1°. However, before interpolation, we applied a 5x5 pixel mean averaging to fill gaps in the mapped satellite data, considering only values different from zero. Otherwise, the linear interpolation would have led to a loss of information when mapping on a coarser grid, because the regular grid is about 4 to 5 times coarser than the retrieval grid. These gaps in the satellite data arise during mapping from the native format onto a regular lat-lon grid as needed for the SAL analysis and are due to the increasing pixel sizes towards the edges of the retrieval domain.

To define objects in the SAL analysis, we used a threshold of 0.2 g m^{-2} for modeled and observed ash, because this is the detection threshold for the Himawari-8 ash retrievals. For SO_2, a threshold of 2.5 g m^{-2} for model and observations is used to remove background SO_2 concentrations in Himawari-8 data. This was necessary, because we did not initialize the model with realistic background conditions and, therefore, can only compare the observed and modeled SO_2 plume from the eruption.

3 Results and discussions

3.1 Validation of mass loading

The Raikoke eruption 2019 injected ash and SO_2 up to 14 km into the atmosphere. Figure 3 shows mean ash (left) and SO_2 (right) column on June 22, 0-23 UTC (top row) and June 23, 0-23 UTC (bottom row) in our reference simulation FPlume-rad. The volcanic plume first spreads with westerly winds and is then dragged into a low pressure system over the Northern Pacific Ocean. In the mass loadings of both compounds, no clear horizontal separation of the ash and SO_2 plume is visible (compare

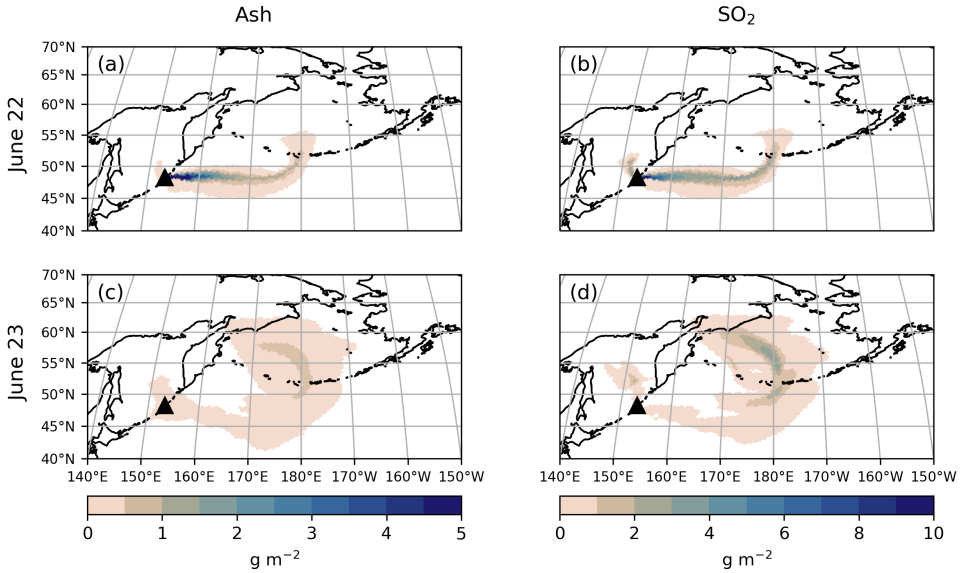

Figure 3. Simulated daily mean column mass loadings for ash (left) and SO_2 (right) on June 22, 2019 0-23 UTC (top row) and June 23, 2019 0-23 UTC (bottom row) in g m^{-2}. The results are based on the FPlume-rad experiment.

Fig. 3 left and right side). However, we will further investigate the separation of ash and SO_2 due to radiation in Sect. 3.3 after we validated our setup.

Figure 4a shows the temporal evolution of the ash loading in the atmosphere following the Raikoke eruption for different experiments and observations. The temporal resolution of the data is 1h. The Himawari-8 data reveals a steep increase of ash mass at 22 UTC on June 21 until a peak of 1.0 Tg is reached at 5 UTC on June 22 and the curve remains above 1.0 Tg for 5 hours. The maximum at 7 UTC (June 22) of 1.1 Tg is followed by a descent to 0.3–0.5 Tg.

M20 (green curve) emphasized that aerosol processes account for the ash removal. Nucleation, condensation, and coagulation increase the size of aerosol particles and, thus, lead to a faster sedimentation. However, M20 were not able to quantitatively explain the time lag between model and observations during the first hours of the eruption (18 UTC on June 21 until 3 UTC on June 22). Besides, the continuous emission with a constant MER led to a slight overestimation of the ash mass loading (M20). We have closed these gaps as follows.

The maximum of total ash derived with ICON-ART coupled with FPlume (online treatment) in both experiments with and without radiation-aerosol interaction coincides very well with the Himawari-8 data (in Fig. 4 compare red and yellow curve with black curve). The total ash derived with Mastin (different MER but the same fine ash fractions and emission profile as in the FPlume experiments) overestimates the amount of ash during the first 12 h after the onset of the eruption (blue curve). Thus, neglecting meteorological effects and other plume-related processes in the case of the Raikoke eruption (offline treatment), as

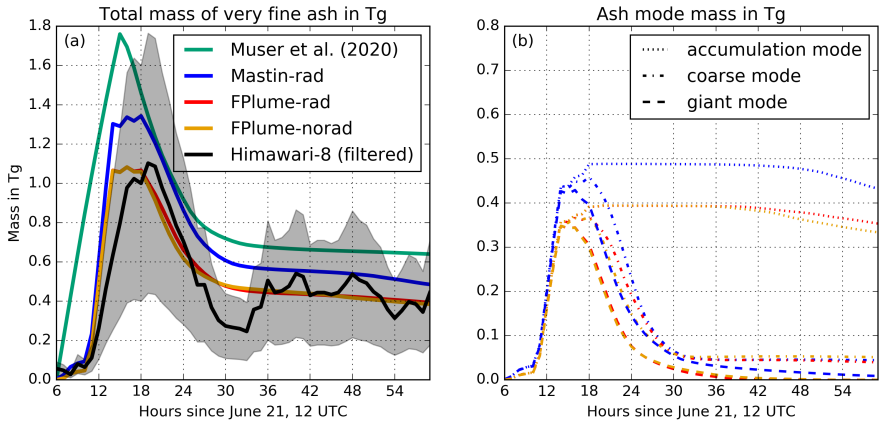

Figure 4. (a): Temporal evolution of the total amount of very fine ash in the atmosphere in Tg for Himawari-8 observations (black) with an estimated uncertainty range (gray shading), simulated by M20 with one constant emission phase (green), simulated with ICON-ART with and without aerosol-radiation interaction, each with phase-dependent FPlume MERs, and a very fine ash fraction derived with the relationship by Gouhier et al. (2019) (red and yellow), and simulated with ICON-ART, eruption-phase dependent Mastin MERs, and the same very fine ash fraction as for the red curve (blue). (b): Temporal evolution of the simulated mass for the different ash modes (dotted: accumulation mode; dash-dotted: coarse mode; dashed: giant modes). The colors refer to the model experiment shown in the left panel.

it is often done in volcanic dispersion forecasts, results in higher MER especially in the long continuous phase of the eruption and subsequently increased ash emissions into ICON-ART (Fig. 2).

All simulation experiments in Fig. 4a include aerosol dynamics and have correctly reproduced the fallout of particles as indicated by the decrease of ash after two days. From Fig. 4b, where the temporal development of the different modes is shown, we can conclude that the decrease of ash after two days is mainly due to coarse and giant mode particles. The total ash from the simulations with FPlume display the best agreement with the Himawari-8 data in this analysis (Fig. 4a). However, the other curves remain mostly within the error range of Himawari-8 data as well (gray shading). Thus, we conclude that the online treatment of plume development improves the ash loading prediction during the first hours and days after the eruption. After about 30 h, the aerosol dynamical processes become more important, and the differences between the experiments decrease.

3.2 Validation of dispersion using SAL

For the quantitative validation of the forecast quality, we performed a SAL analysis using 6 h-averaged SO_2 and ash mass loadings. We compare the results of FPlume-rad experiment and Himawari-8 satellite data. Figure 5 shows the values for the structure on the abscissa, the amplitude on the ordinate, and the location in colors.

The location of the SO_2 plume agrees very well between model and observations throughout the whole simulation period. This is shown by the location values which are close to zero. The structure and amplitude values are close to zero between 24 to 72 hours after the beginning of the simulation on June 21 at 12 UTC. Thus, there is a high agreement between model and

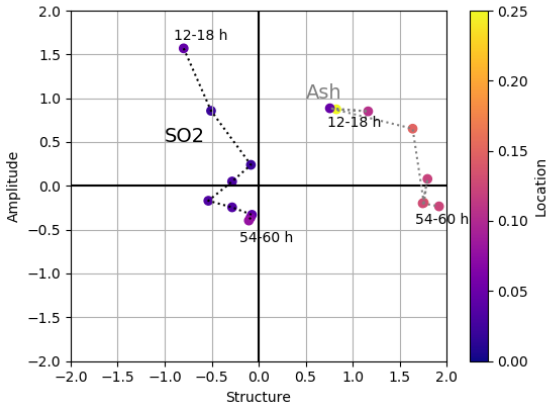

Figure 5. SAL values for ash and SO_2 in the reference experiment (FPlume-rad): with S(tructure) on the abscissa, A(mplitude) on the ordinate, and L(ocation) in colors. The dotted lines connect consecutive hours to visualize the temporal development (black for SO_2 and gray for ash). The labels of the hours are given relative to the start of the simulation on June 21, 2019 at 12 UTC.

observations during this period. However, during the first 24 hours, the model prediction shows higher amplitude values and a low structure value, indicating a larger mass loading in the model and a less diffuse SO_2 plume in the model compared to the satellite estimates. We argue that the discrepancy in the amplitude between model and observation during the first hours of the Raikoke eruption stems from the possible underestimation of SO_2 by the satellite retrievals due to the dense ash plume covering the region around the volcano. In addition, our simulation is also affected by the uncertainties of input parameters (e.g., start and end time of individual eruption phases, plume heights, exit conditions).

The model also predicts the location of the ash plume very well (Fig. 5). The positive structure values indicate that the modeled ash loading becomes more diffusive over the domain for most of the time. Fig. A3 (first and second column) compares all 6 h–mean ash loadings. The large spread of the modeled ash plume across large parts of the northern Pacific Ocean is not seen in the observations, which is the main reason for the high structure value in Fig. 5. We argue that Himawari-8 measurements of ash at this time might be hampered by water and ice clouds overlapping and obscuring the ash plume. This argument further explains why the temporal evolution of the Himawari-8 measurements in Fig. 4a shows variations between 30 and 60 h although the emission from Raikoke ceased.

The high amplitude value for ash between 12 and 36 h, despite the almost perfect agreement in the total mass in Fig. 4, also stems from the larger spread of the ash plume in the beginning. The reason is that the background values are considered zero and the Amplitude in the SAL analysis, unlike the object-based structure and location values, is a domain-averaged quantity.

We have shown that the model setup realistically represents the amount of ash following the Raikoke 2019 eruption and the dispersion of the ash and SO_2 agrees well with the observations. In the next step, we analyse the vertical distribution of the ash and SO_2 plume.

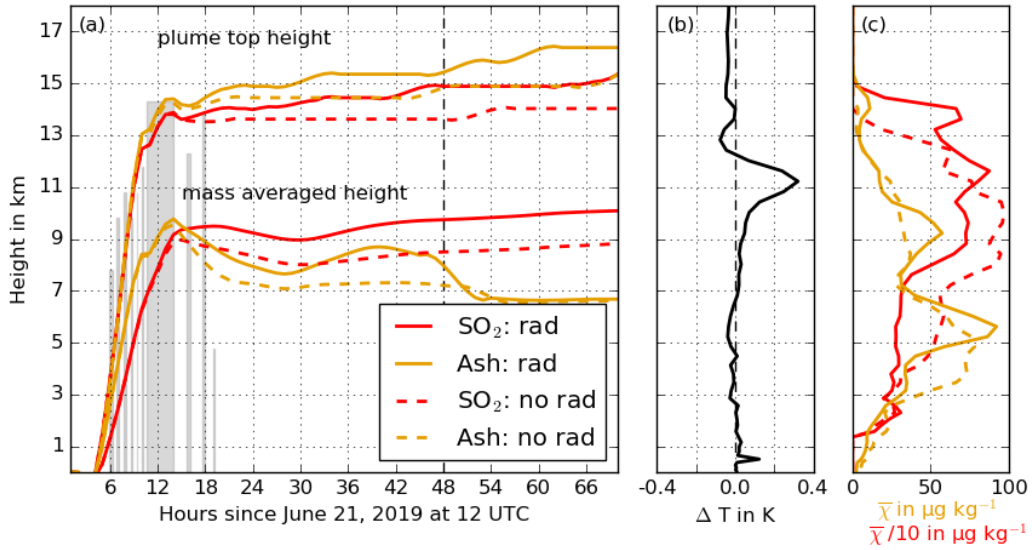

Figure 6. (a): Temporal evolution of the SO_2 (red) and ash (yellow) plume top height and mass–averaged height for the FPlume-rad (solid) and FPlume-norad (dashed) experiment smoothed by a Savitzky-Golay filter. The gray bars indicate the duration and height of the 10 individual eruption phases. They are based on the analysis of the GOES-17 data, which serve as inputs for FPlume; (b): vertical profile of the temperature difference between the FPlume-rad and FPlume-norad in the ash plume 48 h after the start of the simulation. (c): vertical SO_2 (red) and ash (yellow) profile after 48 h for the FPlume-rad (solid) and FPlume-norad (dashed) experiment.

3.3 Vertical separation of SO_2 and ash plume

In this section, we discuss the evolution of the ash and SO_2 plume top heights and focus on the radiative effects on the plume dynamics.

Figure 6 shows the top height of the ash and SO_2 plume for the FPlume-rad and FPlume-norad experiment (a), the resulting vertical temperature difference on June 23, 12 UTC (b), and the vertical distribution of SO_2 and ash mixing ratios on the same date (c). The plume top height in a) is defined as the maximum height of all grid cells in the plume that were separated from background mixing ratios as explained in Sect. 2.2.1. The average plume height in a) is the mean height weighted by the mass of all grid cells that are considered inside the plume. The values in b) and c) were horizontally averaged over the whole detected plume, again excluding grid cells outside the plume. In b) and c), we picked June 23, 12 UTC, because it allows a direct comparison to Fig. 8 in M20, which only shows the ash plume top height. The lines for the plume top height and mass averaged height are smoothed by a Savitzky-Golay filter to remove 'steps' due to the low vertical resolution at upper atmospheric model levels. The difference in height between FPlume-rad and FPlume-norad remains similar, regardless of the use of this filter.. However, the increasing plume height already starting before the beginning of the eruption is a result of the filtering.

During the first hours after the beginning of the eruption, the plume top height for ash and SO_2 mainly rises due to the higher eruption heights of later eruption phases. The gray bars, which indicate the eruption height, coincide well with the top height (Fig. 6a).

Shortly after the end of the long eruption phase, we clearly see a separation of the ash plume top height between the FPlume-rad and the FPlume-norad experiments. The effect of the ash lofting due to radiation was already investigated in detail by M20 with the same model system. They found that the absorption of shortwave and longwave radiation by the coated ash particles leads to the warming and rising of the ash plume. We compare the vertical profile of the temperature difference between the FPlume-rad and FPlume-norad case here with the vertical temperature differences in M20 on June 23, 12 UTC. A single large positive anomaly of approximately 0.3 K near 11 km occurs in our simulation (Fig. 6b). Subsequently, the whole ash plume rises to higher altitudes. In contrast, M20 found two distinct temperature anomaly peaks around 10 km and 14 km in the order of 0.25 K each, which result in the formation of two maxima in the ash mixing ratios near 10 km and 15 km. The resulting uplift during the first 12 h in the ash plume in our simulation is about 33% of the resulted lifting in M20.

In the first hours during and after the eruption, the absorption-induced warming of the ash plume also causes the SO_2 plume to rise in FPlume-rad (Fig. 6a and c). However, as SO_2 itself absorbs neither solar nor terrestrial radiation in our model setup, the ash plume top height clearly separates from the SO_2 plume top height with increasing time (Fig. 6a). The vertical profiles of the SO_2 mixing ratio in the FPlume-rad and FPlume-norad case indicate that radiation interaction smooths and reduces the vertical gradient of the SO_2 mixing ratios in the troposphere. In the stratosphere, a second peak occurs above the maximum emission height (Fig. 6c).

The evolution of the mass–averaged height of the ash and SO_2 plume indicate an opposite behavior than the plume top height. The mass average of the SO_2 plume is generally higher than for the ash plume. In Fig. 7a and c, the vertical distribution of the ash and SO_2 mass concentrations in kg m^{-3} confirm that the SO_2 plume is about 5 km higher on average than the ash plume after three days. This is in agreement with several existing studies (e.g., Timmreck, 2012; Robock, 2000), which emphasized a fast removal of ash after volcanic eruptions related to the higher weight of ash particles compared to SO_2. The step-wise reduction of the ash in the mass averaged height is related to the loss of the giant mode during the first 24 h and the a large fallout of the coarse mode until about 50 h relative to simulation start (Fig. 4b and Fig. A4).

In the next step, we want to compare the vertical distribution of a characteristic ash particle radius $\overline{R}$, which we calculated as follows:

$$\overline{R} = \frac{\sum_{i=1}^{5} r_{m,i} \cdot N_i}{\sum_{i=1}^{5} N_i} \tag{5}$$

For the overall characteristic radius $\overline{R}$, we consider the five ash modes $i = 1,5$ (insoluble and mixed accumulation mode, insoluble and mixed coarse mode, and giant mode) and calculated $\overline{R}$ at every grid cell. r_m is the median radius from the log normal distribution and N is the number of particles per grid box. The vertical distribution of the horizontally averaged characteristic radius in Fig. 7b also shows the loss of the larger particles (coarse and giant mode) during the first 24 h. Afterwards, the values

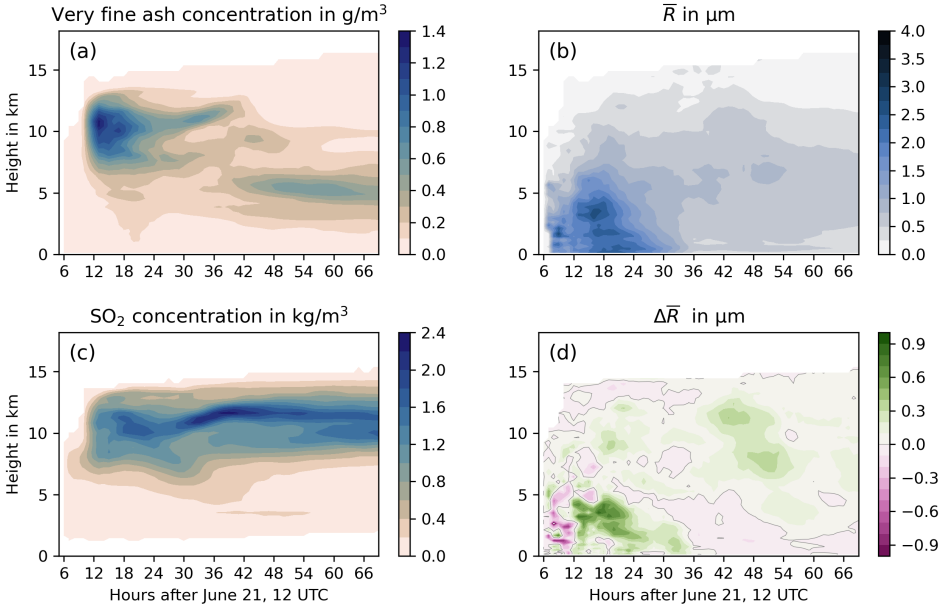

Figure 7. Left: Temporal evolution of the horizontally averaged vertical distribution of ash mass concentration (a) and SO_2 mass concentration (c) in the FPlume-rad experiment. Right: number-weighted characteristic ash radius (Eq. 5) for FPlume-rad (b) and difference between FPlume-rad and FPlume-norad (d).

of the mean characteristic radius are below 1.5 μm with a maximum around 5 to 6 km. In comparison to the FPlume-norad experiment, the characteristic radius is higher on average compared to the FPlume-rad experiments because aerosol radiation–interaction slows down the removal of larger particles from the atmosphere (Fig. 7d). This effect is visible in the removal of the accumulation mode, which is reduced in FPlume-rad (Fig. 4b). Compared to the FPlume-norad, the removal of the coarse modes in FPlume-rad is delayed by about 1 h between 18 and 25 h after the simulation start (Fig 4b). After about 30 h the amount of the coarse mode is slightly lower in the FPlume-rad than in FPlume-norad, because the particle radius is larger at most altitudes (Fig 4b and Fig. 7d). The temporal removal of the giant mode only shows small differences between FPlume-rad and FPlume-norad (Fig. 4b). The larger mean characteristic radius after approximately 48 h is related to an increasing removal of accumulation mode particles in FPlume-norad compared with FPlume-rad (Fig. 7d and Fig. 4b). However, we will leave a detailed analysis of the processes changing particle radii to further work.

Both the main SO_2 mass and the main ash mass are restricted to a narrower vertical range after three simulation days compared the end of the eruption (around 13 h after simulation start). The location of the SO_2 is between 8 and 14 km and between 4 and 7 km for ash (Fig. 7). Thus, for initializing long-range and climate simulations, a release of SO_2 and ash at these altitudes is justified if the sedimentation during the first hours is considered in the total emission rate.

Despite the clear vertical separation of the ash and SO_2 plume, the horizontal separation in both model and observations remains small in the first three days after the eruption. Nevertheless, a strong vertical wind shear can result in the horizontal separation of the ash and SO_2 plume on longer time scales as in Kloss et al. (2021).

4 Conclusions

We investigated the Raikoke 2019 eruption, which was characterized by nine shorter eruption phases and one continuous eruption phase of almost 3-hour-duration. Here, we describe a model setup in which the ESPs were improved by (1) coupling ICON-ART with FPlume to account for the effect of changing volcanic and meteorological conditions and (2) a delineation of eruption phases. We further investigated the effect of radiation-aerosol interaction on the SO_2 plume due to a warming of the ash plume. The main findings are:

1. We demonstrated a large improvement of the total ash burden forecast in the first 12 h by resolving the individual eruption phases of the Raikoke eruption, which reduces the ash mass overestimation from 37% to 18%. Additionally, the online calculation of ESPs by FPlume further improves temporal evolution of the simulated ash mass, which shows an almost perfect agreement with the observed evolution of ash mass loading.

2. In addition to the mass loading, the predicted spatial dispersion of the ash and SO_2 plume also agrees well with observations from Himawari-8 as our SAL analysis reveals. However, we hypothesize that the validation of the simulated ash and SO_2 dispersion is partially hampered by a dense ash plume in the beginning of the eruption and by overlapping water and ice clouds later on.

3. As already demonstrated in M20, aerosol radiation interaction leads to a warming of the volcanic ash plume and, therefore, to a lofting of ash particles during the first hours. Here, we additionally found a lofting of the SO_2 plume during the first 12 h after the eruption caused by a warming of the plume. However, with increasing time, the SO_2 plume becomes more and more vertically separated from the ash plume and the lofting slows down. This is related to a faster sedimentation of the ash particles compared to SO_2 and the fact that SO_2 does not absorb solar radiation in our model.

Code and data availability. The output from ICON-ART simulations performed in this study can be provided upon request by the corresponding author. The ICON-ART code is licence protected and can be accessed by request to the corresponding author. Himawari-8 AHI datasets that have been analyzed in the scope of this study can be provided upon request by the corresponding author.

Author contributions. JB, GAH, LOM, CH, BV developed the ICON-ART code and carried out simulations. ÁH provided plume heights and durations based on GOES-17 data. FJP processed the Himawari-8 data, did the ash and SO_2 retrievals. JB and GAH prepared the paper with significant contributions and comments on the original draft from all authors.

Competing interests. The authors declare that they have no conflict of interest.

Disclaimer.

Acknowledgements. This research has been funded by the Deutsche Forschungsgemeinschaft (DFG) as part of the Research Unit VolImpact (FOR2820, DFG Grant No.398006378). The contributions are within the VolImpact sub-projects VolPlume (JB, GAH, BV and ÁH) and VolCloud (CH). JMA/JAXA are acknowledged for providing Himawari-8 data. We thank Fabio Crameri for the development of scientific colour maps (Crameri, 2021) to prevent visual distortion of the data and exclusion of readers with colour-vision defencies (Crameri et al., 2020). Furthermore, we acknowledge support by the KIT Publication Fund of the Karlsruhe Institute of Technology.

References

Beckett, F. M., Witham, C. S., Leadbetter, S. J., Crocker, R., Webster, H. N., Hort, M. C., Jones, A. R., Devenish, B. J., and Thomson, D. J.: Atmospheric dispersion modelling at the London VAAC: A review of developments since the 2010 eyjafjallajökull volcano ash cloud, Atmosphere, 11, https://doi.org/10.3390/atmos11040352, 2020.

Brown, R. J., Bonadonna, C., and Durant, A. J.: A Review of Volcanic Ash Aggregation, Physics and Chemistry of the Earth, A/B/C, 65–78, 2012.

Casadevall, T. J.: Volcanic ash and aviation safety: Proceedings of the first international symposium on volcanic ash and aviation safety, U.S. Geological Survey, https://doi.org/10.3133/b2047, 1994.

Collini, E., Osores, M. S., Folch, A., Viramonte, J., Villaosa, G., and Salmuni, G.: Volcanic ash forecast during the June 2011 Cordón Caulle eruption, Natural Hazards, 66, 389–412, https://doi.org/10.1007/s11069-012-0492-y, 2013.

Crameri, F.: Scientific colour maps Version 7.0.0 (February 2021), https://doi.org/10.5281/zenodo.4491293, 2021.

Crameri, F., Shephard, G. E., and Heron, P. J.: The misuse of colour in science communication, Nature Communications, 11, https://doi.org/https://doi.org/10.1038/s41467-020-19160-7, 2020.

De Leeuw, J., Schmidt, A., Witham, C. S., Theys, N., Taylor, I. A., Grainger, R. G., Pope, R. J., Haywood, J., Osborne, M., and Kristiansen, N. I.: The 2019 Raikoke volcanic eruption – Part 1: Dispersion model simulations and satellite retrievals of volcanic sulfur dioxide, Atmospheric Chemistry and Physics Discussions, 2020, 1–38, https://doi.org/10.5194/acp-2020-889, 2020.

Degruyter, W. and Bonadonna, C.: Improving on mass flow rate estimates of volcanic eruptions, Geophysical Research Letters, 39, https://doi.org/10.1029/2012GL052566, 2012.

Folch, A., Costa, A., and Macedonio, G.: FPLUME-1.0: An integral volcanic plume model accounting for ash aggregation, Geoscientific Model Development, 9, 431–450, https://doi.org/10.5194/gmd-9-431-2016, 2016.

Giorgetta, M. A., Brokopf, R., Crueger, T., Esch, M., Fiedler, S., Helmert, J., Hohenegger, C., Kornblueh, L., Köhler, M., Manzini, E., Mauritsen, T., Nam, C., Raddatz, T., Rast, S., Reinert, D., Sakradzija, M., Schmidt, H., Schneck, R., Schnur, R., Silvers, L., Wan, H., Zängl, G., and Stevens, B.: ICON-A, the Atmosphere Component of the ICON Earth System Model: I. Model Description, Journal of Advances in Modeling Earth Systems, 10, 1613–1637, https://doi.org/https://doi.org/10.1029/2017MS001242, 2018.

Gouhier, M., Eychenne, J., Azzaoui, N., Guillin, A., Deslandes, M., Poret, M., Costa, A., and Husson, P.: Author Correction: Low efficiency of large volcanic eruptions in transporting very fine ash into the atmosphere (Scientific Reports, (2019), 9, 1, (1449), 10.1038/s41598-019-38595-7), Scientific Reports, 9, 1–12, https://doi.org/10.1038/s41598-019-42489-z, 2019.

Harvey, N. J., Huntley, N., Dacre, H. F., Goldstein, M., Thomson, D., and Webster, H.: Multi-level emulation of a volcanic ash transport and dispersion model to quantify sensitivity to uncertain parameters, Natural Hazards and Earth System Sciences, 18, 41–43, https://doi.org/10.5194/nhess-18-41-2018, 2018.

Heinze, R., Dipankar, A., Henken, C. C., Moseley, C., Sourdeval, O., Trömel, S., Xie, X., Adamidis, P., Ament, F., Baars, H., Barthlott, C., Behrendt, A., Blahak, U., Bley, S., Brdar, S., Brueck, M., Crewell, S., Deneke, H., Di Girolamo, P., Evaristo, R., Fischer, J., Frank, C., Friederichs, P., Göcke, T., Gorges, K., Hande, L., Hanke, M., Hansen, A., Hege, H.-C., Hoose, C., Jahns, T., Kalthoff, N., Klocke, D., Kneifel, S., Knippertz, P., Kuhn, A., van Laar, T., Macke, A., Maurer, V., Mayer, B., Meyer, C. I., Muppa, S. K., Neggers, R. A. J., Orlandi, E., Pantillon, F., Pospichal, B., Röber, N., Scheck, L., Seifert, A., Seifert, P., Senf, F., Siligam, P., Simmer, C., Steinke, S., Stevens, B., Wapler, K., Weniger, M., Wulfmeyer, V., Zängl, G., Zhang, D., and Quaas, J.: Large-eddy simula-

tions over Germany using ICON: a comprehensive evaluation, Quarterly Journal of the Royal Meteorological Society, 143, 69–100, https://doi.org/https://doi.org/10.1002/qj.2947, 2017.

Horváth, A., Carr, J. L., Girina, O. A.and Wu, D. L., Bril, A. A., Mazurov, A. A., Melnikov, D. V., Hoshyaripour, G. A., and A., B. S.: Geometric estimation of volcanic eruption column height from GOES-R near-limb imagery – Part 1: Methodology, Atmospheric Chemistry and Physics, 21, 12 189–12 206, https://doi.org/10.5194/acp-21-12189-2021, 2021a.

Horváth, A., Girina, O. A., Carr, J. L., Wu, D. L., Bril, A. A., Mazurov, A. A., Melnikov, D. V., Hoshyaripour, G. A., and A., B. S.: Geometric estimation of volcanic eruption column height from GOES-R near-limb imagery – Part 2: Case studies, Atmospheric Chemistry and Physics, 21, 12 207–12 226, https://doi.org/10.5194/acp-21-12207-2021, 2021b.

Horwell, C. J. and Baxter, P. J.: The respiratory health hazards of volcanic ash: A review for volcanic risk mitigation, Bulletin of Volcanology, 69, 1–24, https://doi.org/10.1007/s00445-006-0052-y, 2006.

Jensen, E. J., Woods, S., Lawson, R. P., Bui, T. P., Pfister, L., Thornberry, T. D., Rollins, A. W., Vernier, J.-P., Pan, L. L., Honomichl, S., and Toon, O. B.: Ash Particles Detected in the Tropical Lower Stratosphere, Geophysical Research Letters, 45, 11,483–11,489, https://doi.org/https://doi.org/10.1029/2018GL079605, 2018.

Kloss, C., Berthet, G., Sellitto, P., Ploeger, F., Taha, G., Tidiga, M., Eremenko, M., Bossolasco, A., Jégou, F., Renard, J.-B., and Legras, B.: Stratospheric aerosol layer perturbation caused by the 2019 Raikoke and Ulawun eruptions and their radiative forcing, Atmospheric Chemistry and Physics, 21, 535–560, https://doi.org/10.5194/acp-21-535-2021, 2021.

Macedonio, G., Costa, A., and Folch, A.: Uncertainties in volcanic plume modeling: A parametric study using FPLUME, Journal of Volcanology and Geothermal Research, 326, 92–102, https://doi.org/10.1016/j.jvolgeores.2016.03.016, 2016.

Marti, A., Folch, A., Jorba, O., and Janjic, Z.: Volcanic ash modeling with the online NMMB-MONARCH-ASH v1.0 model: Model description, case simulation, and evaluation, Atmospheric Chemistry and Physics, 17, 4005–4030, https://doi.org/10.5194/acp-17-4005-2017, 2017.

Mastin, L. G.: A user-friendly one-dimensional model for wet volcanic plumes, Geochemistry, Geophysics, Geosystems, 8, https://doi.org/https://doi.org/10.1029/2006GC001455, 2007.

Mastin, L. G., Guffanti, M., Servranckx, R., Webley, P., Barsotti, S., Dean, K., Durant, A., Ewert, J. W., Neri, A., Rose, W. I., Schneider, D., Siebert, L., Stunder, B., Swanson, G., Tupper, A., Volentik, A., and Waythomas, C. F.: A multidisciplinary effort to assign realistic source parameters to models of volcanic ash-cloud transport and dispersion during eruptions, Journal of Volcanology and Geothermal Research, 186, 10–21, https://doi.org/10.1016/j.jvolgeores.2009.01.008, 2009.

Mather, T. a.: Volcanism and the atmosphere: the potential role of the atmosphere in unlocking the reactivity of volcanic emissions., Philosophical transactions. Series A, Mathematical, physical, and engineering sciences, 366, 4581–4595, https://doi.org/10.1098/rsta.2008.0152, 2008.

Morton, B. R., Taylor, G., and Turner, J. S.: Turbulent Gravitational Convection from Maintained and Instantaneous Sources, Proceedings of the Royal Society of London Series A, 234, 1–23, https://doi.org/10.1098/rspa.1956.0011, 1956.

Muser, L. O., Hoshyaripour, G. A., Bruckert, J., Horváth, A., Malinina, E., Wallis, S., Prata, F. J., Rozanov, A., von Savigny, C., Vogel, H., and Vogel, B.: Particle aging and aerosol–radiation interaction affect volcanic plume dispersion: evidence from the Raikoke 2019 eruption, Atmospheric Chemistry and Physics, 20, 15 015–15 036, https://doi.org/10.5194/acp-20-15015-2020, 2020.

Niemeier, U., Timmreck, C., Graf, H.-F., Kinne, S., Rast, S., and Self, S.: Initial fate of fine ash and sulfur from large volcanic eruptions, Atmospheric Chemistry and Physics, 9, 9043–9057, https://doi.org/10.5194/acp-9-9043-2009, 2009.

Plu, M., Bigeard, G., Sič, B., Emili, E., Bugliaro, L., El Amraoui, L., Guth, J., Josse, B., Mona, L., and Piontek, D.: Modelling the volcanic ash plume from Eyjafjallajökull eruption (May 2010) over Europe: evaluation of the benefit of source term improvements and of the assimilation of aerosol measurements, Natural Hazards and Earth System Sciences Discussions, 2021, 1–24, https://doi.org/10.5194/nhess-2021-97, submitted, 2021.

Prata, A., Rose, W., Self, S., and O'Brien, D.: Global, Long-Term Sulphur Dioxide Measurements from TOVS Data: A New Tool for Studying Explosive Volcanism and Climate, pp. 75–92, American Geophysical Union (AGU), https://doi.org/https://doi.org/10.1029/139GM05, 2004.

Prata, F., Woodhouse, M., Huppert, H. E., Prata, A., Thordarson, T., and Carn, S.: Atmospheric processes affecting the separation of volcanic ash and SO2 in volcanic eruptions: Inferences from the May 2011 Grímsvötn eruption, Atmospheric Chemistry and Physics, 17, 10 709–10 732, https://doi.org/10.5194/acp-17-10709-2017, 2017.

Rieger, D., Bangert, M., Bischoff-Gauss, I., Förstner, J., Lundgren, K., Reinert, D., Schröter, J., Vogel, H., Zängl, G., Ruhnke, R., and Vogel, B.: ICON-ART 1.0 - A new online-coupled model system from the global to regional scale, Geoscientific Model Development, 8, 1659–1676, https://doi.org/10.5194/gmd-8-1659-2015, 2015.

Robock, A.: Volcanic Eruptions and Climate, Reviews of Geophysics, 38, 191–219, 2000.

Rose, W. I. and Durant, A. J.: Fine ash content of explosive eruptions, Journal of Volcanology and Geothermal Research, 186, 32–39, https://doi.org/10.1016/j.jvolgeores.2009.01.010, 2009.

Schröter, J., Rieger, D., Stassen, C., Vogel, H., Weimer, M., Werchner, S., Förstner, J., Prill, F., Reinert, D., Giorgetta, M., Ruhnke, R., Vogel, B., and Braesicke, P.: ICON-ART 2.1: A flexible tracer framework and its application for composition studies in numerical weather forecasting and climate simulations, Geoscientific Model Development, 11, 4043–4068, https://doi.org/10.5194/gmd-11-4043-2018, 2018.

Scollo, S., Folch, A., and Costa, A.: A parametric and comparative study of different tephra fallout models, Journal of Volcanology and Geothermal Research, 176, 199–211, https://doi.org/10.1016/j.jvolgeores.2008.04.002, 2008.

Spence, R. J., Kelman, I., Calogero, E., Toyos, G., Baxter, P. J., and Komorowski, J. C.: Modelling expected physical impacts and human casualties from explosive volcanic eruptions, Natural Hazards and Earth System Science, 5, 1003–1015, https://doi.org/10.5194/nhess-5-1003-2005, 2005.

Stewart, C., Johnston, D., Leonard, G., Horwell, C., Thordarson, T., and Cronin, S.: Contamination of water supplies by volcanic ashfall: A literature review and simple impact modelling, Journal of Volcanology and Geothermal Research, 158, 296–306, 2006.

Stuefer, M., Freitas, S. R., Grell, G., Webley, P., Peckham, S., and McKeen, S. a.: Inclusion of Ash and SO2 emissions from volcanic eruptions in WRF-CHEM: development and some applications, Geoscientific Model Development Discussions, 5, 2571–2597, https://doi.org/10.5194/gmdd-5-2571-2012, 2012.

Textor, C., Graf, H.-f., Longo, A., and Neri, A.: Numerical simulation of explosive volcanic eruptions from the conduit flow to global atmospheric scales, ANNALS OF GEOPHYSICS, 48, 2005.

Thomas, H. E. and Prata, A. J.: Sulphur dioxide as a volcanic ash proxy during the April–May 2010 eruption of Eyjafjallajökull Volcano, Iceland, Atmospheric Chemistry and Physics, 11, 6871–6880, https://doi.org/10.5194/acp-11-6871-2011, 2011.

Timmreck, C.: Modeling the climatic effects of large explosive volcanic eruptions, Wiley Interdisciplinary Reviews: Climate Change, 3, 545–564, https://doi.org/10.1002/wcc.192, 2012.

van Eaton, A. R., Muirhead, J. D., Wilson, C. J., and Cimarelli, C.: Growth of volcanic ash aggregates in the presence of liquid water and ice: An experimental approach, Bulletin of Volcanology, 74, 1963–1984, https://doi.org/10.1007/s00445-012-0634-9, 2012.

von Savigny, C., Timmreck, C., Buehler, S. A., Burrows, J. P., Giorgetta, M., Hegerl, G., Horvath, A., Hoshyaripour, G. A., Hoose, C., Quaas, J., Malinina, E., Rozanov, A., Schmidt, H., Thomason, L., Toohey, M., and Vogel, B.: The research unit volimpact: Revisiting the volcanic impact on atmosphere and climate - preparations for the next big volcanic eruption, Meteorologische Zeitschrift, 29, 3–18, https://doi.org/10.1127/metz/2019/0999, 2020.

Wardman, J. B., Wilson, T. M., Bodger, P. S., Cole, J. W., and Stewart, C.: Potential impacts from tephra fall to electric power systems: A review and mitigation strategies, Bulletin of Volcanology, 74, 2221–2241, https://doi.org/10.1007/s00445-012-0664-3, 2012.

Webster, H. N., Thomson, D. J., Johnson, B. T., Heard, I. P. C., Turnbull, K., Marenco, F., Kristiansen, N. I., Dorsey, J., Minikin, A., Weinzierl, B., Schumann, U., Sparks, R. S. J., Loughlin, S. C., Hort, M. C., Leadbetter, S. J., Devenish, B. J., Manning, A. J., Witham, C. S., Haywood, J. M., and Golding, B. W.: Operational prediction of ash concentrations in the distal volcanic cloud from the 2010 Eyjafjallajökull eruption, Journal of Geophysical Research: Atmospheres, 117, https://doi.org/https://doi.org/10.1029/2011JD016790, 2012.

Weimer, M., Schröter, J., Eckstein, J., Deetz, K., Neumaier, M., Fischbeck, G., Hu, L., Millet, D. B., Rieger, D., Vogel, H., Vogel, B., Reddmann, T., Kirner, O., Ruhnke, R., and Braesicke, P.: An emission module for ICON-ART 2.0: Implementation and simulations of acetone, Geoscientific Model Development, 10, 2471–2494, https://doi.org/10.5194/gmd-10-2471-2017, 2017.

Wernli, H., Paulat, M., Hagen, M., and Frei, C.: SAL - A Novel Quality Measure for the Verification of Quantitative Precipitation Forecasts, Monthly Weather Review, 136, 4470 – 4487, https://doi.org/10.1175/2008MWR2415.1, 2008.

Wernli, H., Hofmann, C., and Zimmer, M.: Spatial Forecast Verification Methods Intercomparison Project: Application of the SAL Technique, Weather and Forecasting, 24, 1472 – 1484, https://doi.org/10.1175/2009WAF2222271.1, 2009.

Woodhouse, M. J., Hogg, A. J., Phillips, J. C., and Sparks, R. S. J.: Interaction between volcanic plumes and wind during the 2010 Eyjafjallajökull eruption, Iceland, Journal of Geophysical Research: Solid Earth, 118, 92–109, https://doi.org/10.1029/2012JB009592, 2013.

Zängl, G., Reinert, D., Rípodas, P., and Baldauf, M.: The ICON (ICOsahedral Non-hydrostatic) modelling framework of DWD and MPI-M: Description of the non-hydrostatic dynamical core, Quarterly Journal of the Royal Meteorological Society, 141, 563–579, https://doi.org/10.1002/qj.2378, 2015.

Zhu, Y., Toon, O. B., Jensen, E. J., Bardeen, C. G., Mills, M. J., Tolbert, M. A., Yu, P., and Woods, S.: Persisting volcanic ash particles impact stratospheric SO2 lifetime and aerosol optical properties, Nature Communications, 11, 1–11, https://doi.org/10.1038/s41467-020-18352-5, 2020.

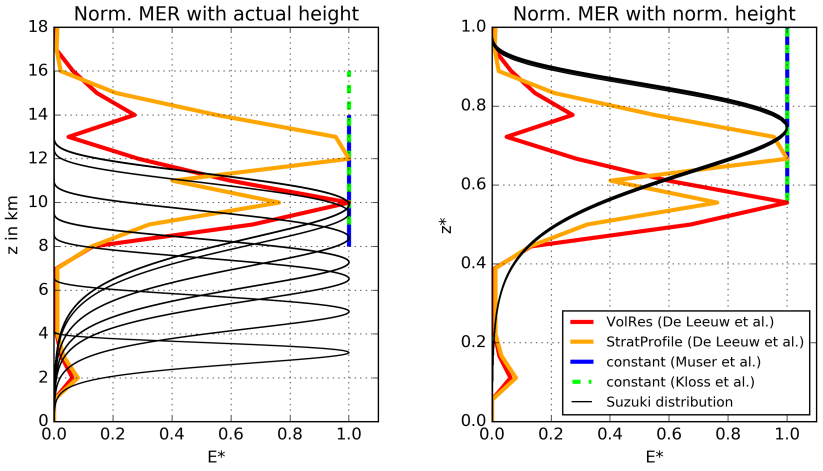

Figure A1. Comparison of Suzuki profile used in this work with profiles from previous studies. Left: Normalized with respect to MER, but with actual emission heights; Right: Normalized with respect to MER and emission height.

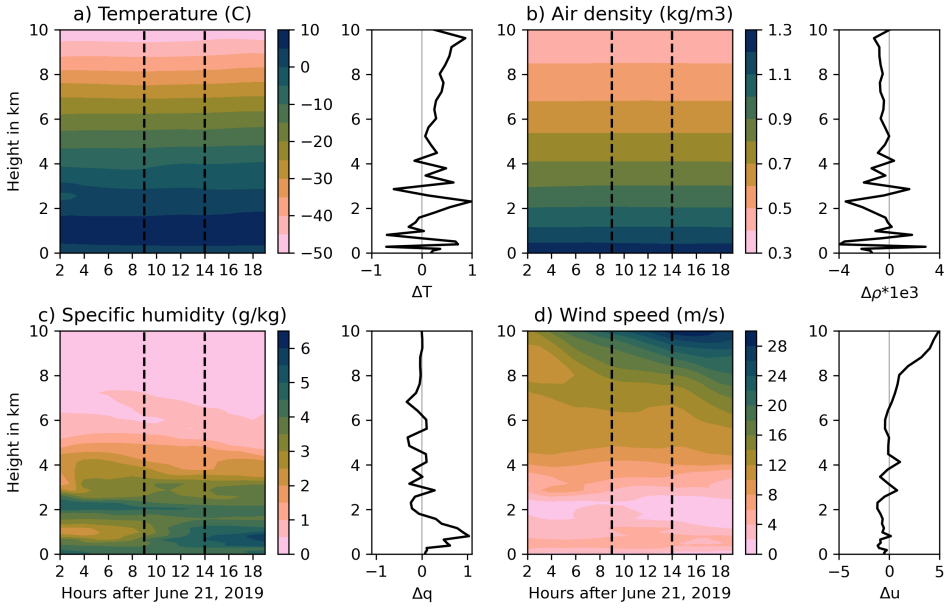

Figure A2. Meteorological conditions above the vent in the first 20 h after simulation start to explain variations in the FPlume-derived MER. Four different atmospheric variables are shown: a) temperature in °C, b) air density in kg m^{-1}, c) specific humidity in g kg^{-1}, and d) the wind speed in m s^{-1}. For each variable the temporal development in the vertical axis above the vent is given over time in contours and the difference between the two time steps indicated by the vertical dashed lines in the contour plot (later step minus earlier time step).

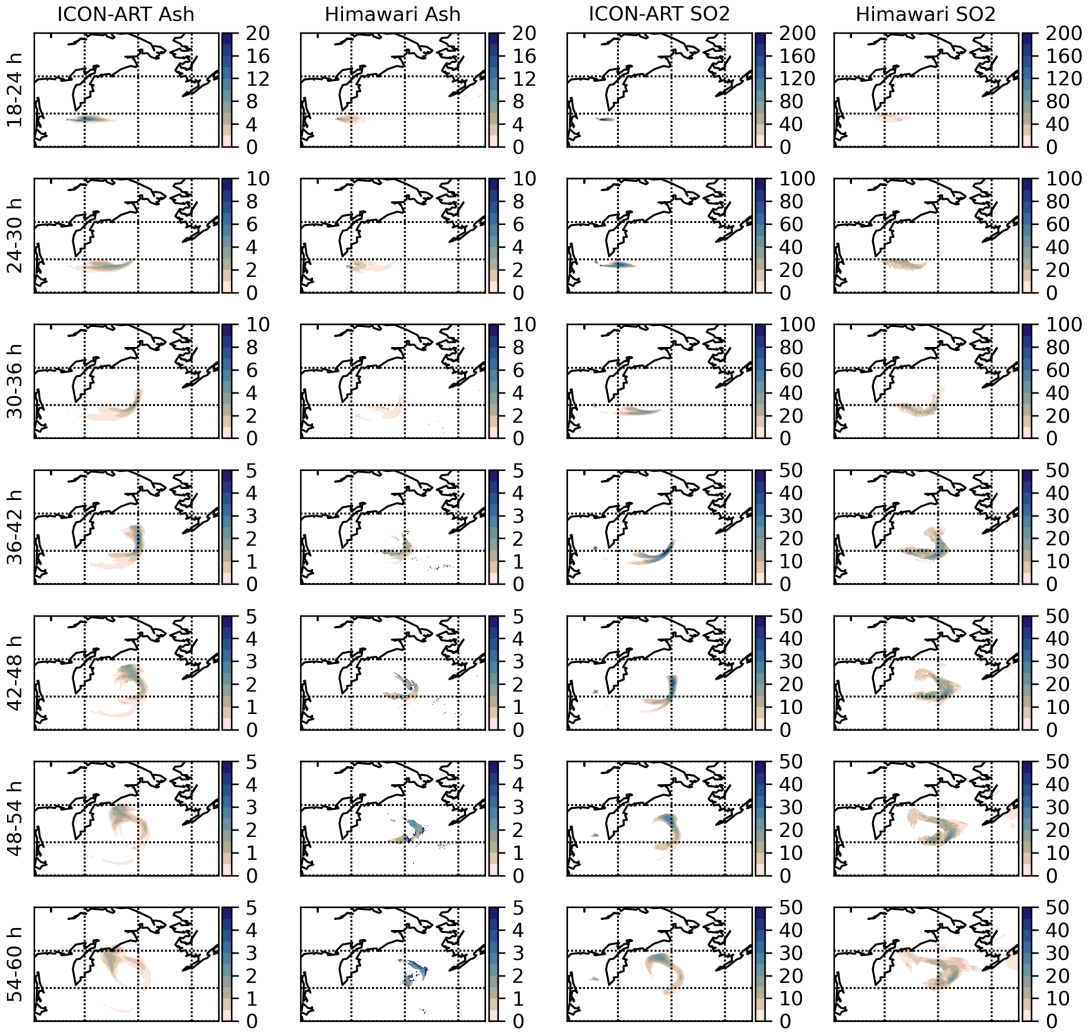

Figure A3. Comparison plots for seven ash and SO_2 6-h averaged column loadings (row 1 to 7) in order to explain the discrepancy between simulated ICON-ART data and Himawari-8 observed data in the SAL analysis. First and second column: ash column loadings in gm^{-2} from ICON-ART and Himawari-8; third and fourth column: SO_2 column loadings in gm^{-2} from ICON-ART and Himawari-8

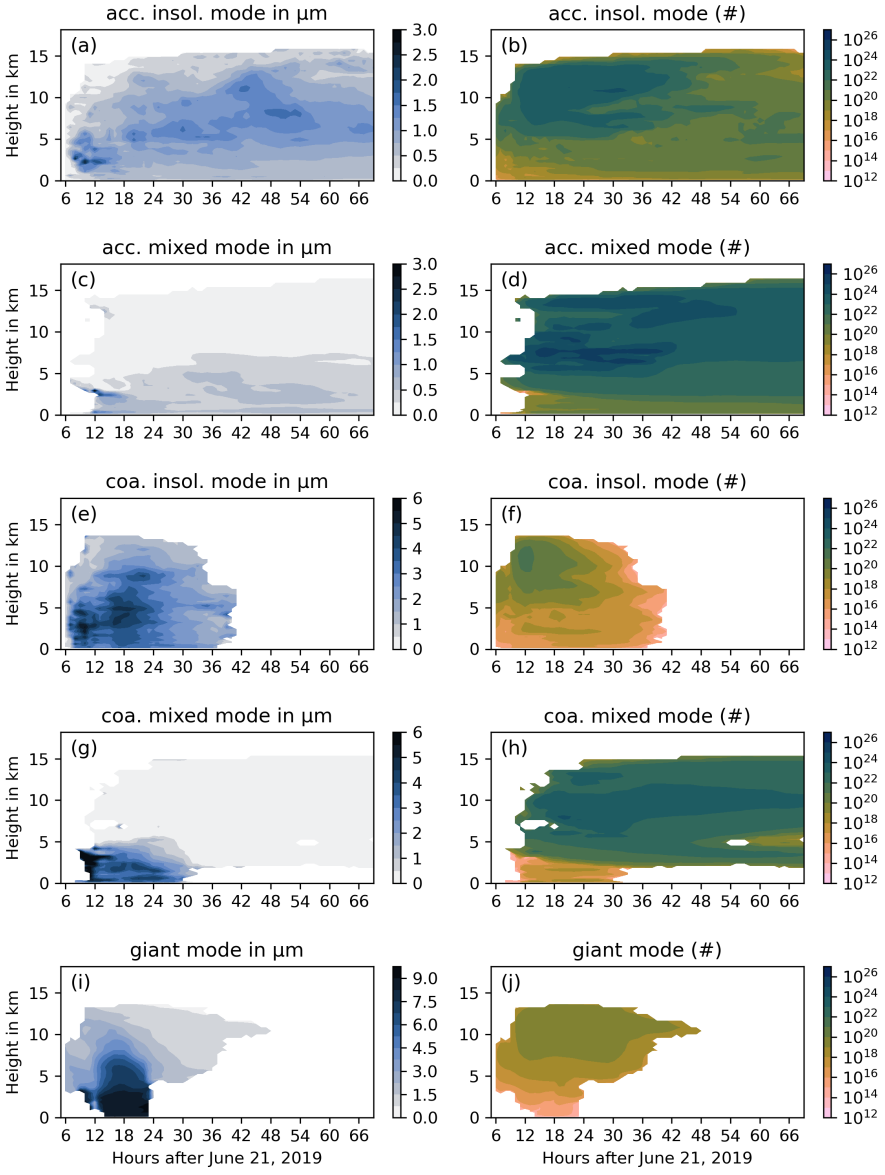

Figure A4. Horizontally averaged ash particle characteristic radius of the log normal distribution in μm (left, Eq. 5) and horizontal sum of the particle number (right) of the different ash modes: insoluble accumulation (a, b), mixed accumulation (c, d), insoluble coarse (e, f), mixed coarse (g, h), and giant mode (i, j).